A novel stick-slip based linear actuator using bi-directional motion of micropositioner

Z. Guo[1], Y. Tian[2, 3], D. Zhang[2], T. Wang[1], M. Wu[1]

[1]Aeronautical Engineering Institute, Civil Aviation University of China, Tianjin 300300, China

[2]Key Laboratory of Mechanism Theory and Equipment Design of Ministry of Education, Tianjin University, Tianjin 300072, China

[3]School of Engineering, University of Warwick, Coventry CV4 7AL, UK

Abstract: A stick-slip based linear actuator was proposed in this paper, which applied the axial motion of the micropositioner to adjust the preload, and the lateral motion to drive the slider. The bi-directional motion of the micropositioner was realized through the asymmetric structure of a flexure-based mechanism, which includes two right circular flexure hinges and four leaf-spring flexure hinges. The static analysis, kinematic analysis and optimization design were successively implemented on the flexure-based mechanism. The Finite Element Analysis (FEA) proved the flexure-based mechanism could generate the bi-directional motion as designed. A prototype of the linear actuator was developed and the measuring system was constructed. A modified sawtooth wave with a cycloid fall curve was designed to improve the output property. The experimental results showed the modified sawtooth wave generated larger velocity than the traditional sawtooth wave in same driving voltages, fall times, driving frequencies and loads. The amplification coefficient and resolution of the proposed linear actuator in single step were 3.16 and 60 nm, respectively. The maximal velocity was 26.2 mm/s with the modified sawtooth wave in driving frequency of 500 Hz.

Keywords: stick-slip, lateral motion, flexure-based mechanism, modified sawtooth wave.

1. Introduction

A motion platform with micro/nano precision is the most important part in the fields of the micro fabrication, micro characteristic and micro operation [1-4]. Among various actuators in precision positioning applications, such as shape memory alloy [5], magnetostrictive actuator [6], voice coil motor [7, 8] and piezoelectric, etc. the piezoelectric is the most popular due to the high resolution, fast response, large stiffness.

Based on the driving principles, the piezoelectric actuators can be divided into

three types: direct driving actuators, inchworm actuators, stick-slip actuators. The direct driving actuators are easy to obtain the nano positioning resolution, but the working space is usually only several micrometers [9-12]. In order to enlarge the stroke, the amplification mechanisms including lever mechanism [13, 14], bridge-type mechanism [15] and Scott-Russell mechanism [16, 17] are designed in the positioning stage. However, the amplification mechanisms make the structure complex, and the stroke is hard to beyond one hundred micrometers. The working principles determine that the inchworm actuators and stick-slip actuators have infinite stroke [18-22]. Generally, the inchworm actuator has larger output force, but it needs several piezoelectric actuators to realize the motion of the clamping mechanism and driving mechanism, which make the structure and control system complex. Such as the positioning stage proposed in reference [20], nine piezoelectric actuators are used to realize the rotation of the central mobile platform. In addition, due to the small stroke of the piezoelectric, the installation precision needs to be very high to realize the clamp and release of the clamping mechanism and slide rail.

In the stick-slip actuator, the slider is driven by using the static and kinematic friction between the slider and stator. In a single step, the static friction force is the driving force in the extension phase, while the kinematic friction force is the resistance in the contraction phase, which generates a backward motion [23-26]. Therefore, the increase of the static friction force and the reduction of the kinematic friction force can improve the output property of the stick-slip actuator. Hunstig adjusted the friction force by change the friction pads and number of magnets [27], but the friction force is constant during the operation. The stick-slip actuator proposed in reference [28] included a bridge-type flexure hinge mechanism and a parallel flexure hinge mechanism, the former could be used to adjust the normal force during the working process, but the overall mechanism is a little bulky. Li [29] used the lateral motion of a parallelogram-type flexure hinge mechanism to design the piezoelectric actuator, the maximal velocity reached 14.25 mm/s, the structure was simple but loose. Cheng [30] proposed a trapezoid-type stick-slip actuator, the lateral motion is realized by the deformation of the trapezoid beam, the normal force could be adjusted by the axial motion, the structure is compact, but the theoretical analysis for this structure is difficult due to the irregularity of the trapezoid beam. The driving signal is another factor to impact the output of the slider, Nguyen [31] optimized the driving signal to reduce the vibration of the slider and suppress the back-step.

A bi-directional output micropositioner is presented based on the proposed

asymmetric flexure-based mechanism, which includes two right circular flexure hinges and four leaf-spring flexure hinges. Further, a stick-slip piezoelectric driven linear actuator is developed. In addition, a modified sawtooth wave with a cycloid fall curve is invented to improve the output property. The components and the working principle of the linear actuator are introduced in section 2. The theoretical modeling and Finite Element Analysis are subsequently implemented for the flexure-based mechanism in sections 3 and 4, respectively. The modified sawtooth wave is firstly displayed in section 5, and then the output property of the slider in the driving of modified sawtooth wave is compared with the traditional sawtooth through various experiments. The experimental results verify that the developed linear actuator was able to realize precision motion, and the modified sawtooth wave has better output properties.

2. Design of the linear actuator

The three-dimensional solid model of the linear actuator is shown in Fig. 1, which mainly includes the micropositioner, slider and preload mechanism. The micropositioner is composed of a flexure-based mechanism, a piezoelectric actuator (PZT) and a preload screw. The flexure-based mechanism is driven by the PZT to generate the axial and lateral motion. The axial motion can dynamically adjust the preload between the micropositioner and the slider, and the lateral motion is utilized to drive the slider move in the *X* direction. The preload screw is applied to preload the piezoelectric and the flexure-based mechanism. The preload mechanism is used to adjust the pressure between the micropositioner and the slider in the initial state.

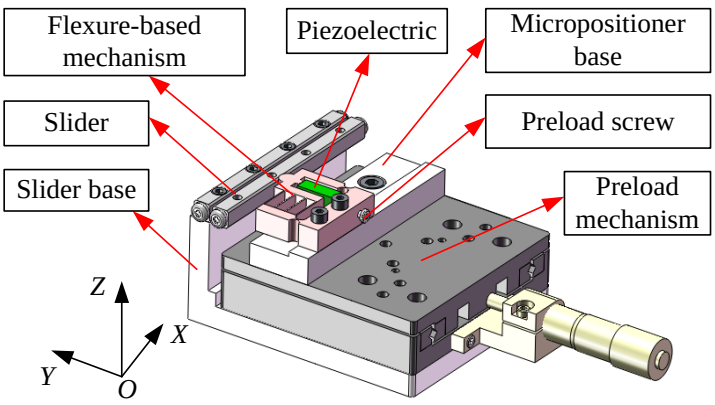

Fig. 1 The three-dimensional model of the linear actuator

As the key part of the linear actuator, the micropositioner is specially shown in Fig. 2. The flexure-based mechanism includes two right circular flexure hinges and

four leaf-spring flexure hinges, which are marked as 1-6 in the Fig. 2. The four leaf-spring flexure hinges are uniformly distributed on the connecting rod 7. The deformation only occurs on the flexure hinges during the operation, the connecting rod 7 and 8 can be seen as rigid. Regarding the axial line of the PZT as the boundary, the right side of the flexure-based mechanism is stiffer than the left side due to the effect of the leaf-spring hinge, thus, the point *O* of flexure-based mechanism generates displacement in both the *Y* direction (axial motion) and *X* direction (lateral motion) when the PZT extends. A half cylinder structure is added between the PZT and the flexible mechanism to eliminate the bending moment acting on the piezoelectric, and the contact area is defined as the driving point. The point *O* is the operating point from the micropositioner to the slider as well as the origin of the global coordinate *O-XYZ*.

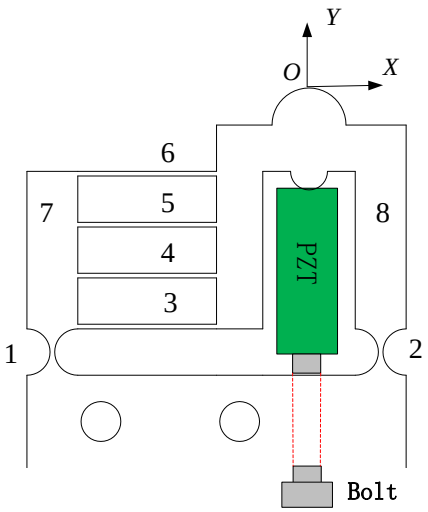

Fig. 2 The micropositioner

Based on the proposed micropositioner, the operating principle is shown in Fig. 3, which is similar to the traditional stick-slip motion. As shown in Fig. 3(a), the micropositioner contacts with the slider in the t_0 phase with an initial pressure.

In the $t_0 - t_1$ phase, the piezoelectric extends slowly with a displacement y, leading to the axial displacement y and lateral displacement x in the point O of the flexure-based mechanism generates, the output of the slider Δ_1 is equal to x due to the stick phenomenon. In this phase, the increase of the axial output displacement raises the pressure between the micropositioner and the slider, and further the static friction force. It is well known that a larger static friction force is good for the stick motion, the slider can be hold tighter, so the actuator has better loading capacity.

In the $t_1 - t_2$ phase, the piezoelectric retracts quickly, the slider generates the backward displacement of Δ_2 due to the kinetic friction force. In this phase, the reduction of the axial displacement leads to the reduction of the pressure and the kinetic friction force. As a result, the backward of the slider is restrained. As shown in Fig. 3(d), the final output of the slider after a single step is

$$\Delta = \Delta_1 - \Delta_2 \tag{1}$$

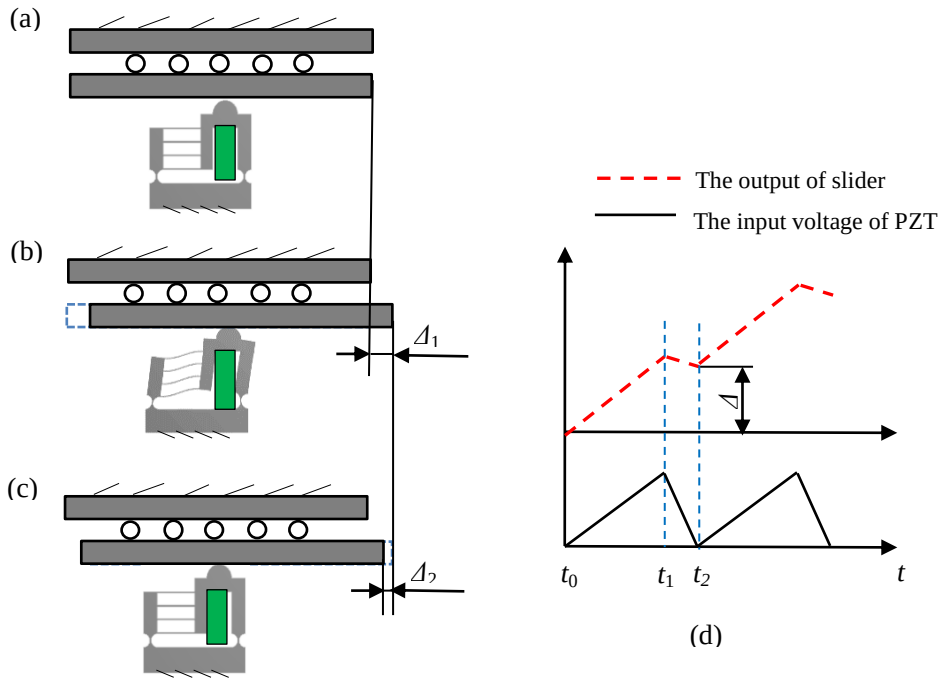

Fig. 3 The operating principle. (a) The t_0 phase. (b) The $t_0 - t_1$ phase. (c) The $t_1 - t_2$ phase. (d) The input of PZT and the output of slider

3. Theoretical modeling of the flexure-based mechanism

3.1 Static analysis

The flexure-based mechanism includes two kinds of flexure hinges: the right circular flexure hinge and the leaf-spring flexure hinge, which are shown in Fig. 4. The compliance matrix has been widely used in the static modeling of the flexure-based mechanisms [7-10, 15], and it has shown good property in the application, so this method is selected in this paper. The compliance matrixes C_{0c} and C_{0l} of the right circular flexure hinge and the leaf-spring flexure hinge in the local coordinate are listed as following equation.

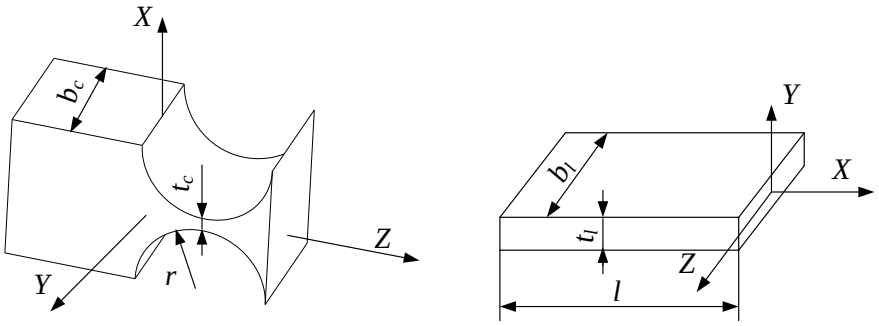

(a) (b)

Fig. 4 Flexure hinges. (a) The right circular flexure hinge. (b) The leaf-spring flexure hinge.

$$C_{0c}=\begin{bmatrix}
\frac{9\pi r^{5/2}}{2Eb_c t_c^{5/2}}+\frac{3\pi r^{3/2}}{2Eb_c t_c^{3/2}} & 0 & 0 & 0 & \frac{9\pi r^{3/2}}{2Eb_c t_c^{5/2}} & 0 \\
0 & \frac{12\pi r^2}{Eb_c^3}\left[\left(\frac{r}{t_c}\right)^{1/2}-\frac{1}{4}\right] & 0 & -\frac{12r}{Eb_c^3}\left[\pi\left(\frac{r}{t_c}\right)^{1/2}-\frac{2+\pi}{2}\right] & 0 & 0 \\
0 & 0 & \frac{1}{Eb_c}\left[\pi\left(\frac{r}{t_c}\right)^{1/2}-\frac{\pi}{2}\right] & 0 & 0 & 0 \\
0 & -\frac{12r}{Eb_c^3}\left[\pi\left(\frac{r}{t_c}\right)^{1/2}-\frac{2+\pi}{2}\right] & 0 & \frac{12}{Eb_c^3}\left[\pi\left(\frac{r}{t_c}\right)^{1/2}-\frac{2+\pi}{2}\right] & 0 & 0 \\
\frac{9\pi r^{3/2}}{2Eb_c t_c^{5/2}} & 0 & 0 & 0 & \frac{9\pi r^{1/2}}{2Eb_c t_c^{5/2}} & 0 \\
0 & 0 & 0 & 0 & 0 & \frac{9\pi r^{1/2}}{4Gb_c t_c^{5/2}}
\end{bmatrix} \tag{2}$$

$$C_{0l}=\begin{bmatrix}
\frac{l}{Eb_l t_l} & 0 & 0 & 0 & 0 & 0 \\
0 & \frac{4l^3}{Eb_l t_l^3} & 0 & 0 & 0 & \frac{6l^2}{Eb_l t_l^3} \\
0 & 0 & \frac{4l^3}{Eb_l^3 t_l} & 0 & -\frac{6l^2}{Eb_l^3 t_l} & 0 \\
0 & 0 & 0 & \frac{l}{Gk_2 b_l t_l^3} & 0 & 0 \\
0 & 0 & -\frac{6l^2}{Eb_l^3 t_l} & 0 & \frac{12l}{Eb_l^3 t_l} & 0 \\
0 & \frac{6l^2}{Eb_l t_l^3} & 0 & 0 & 0 & \frac{12l}{Eb_l t_l^3}
\end{bmatrix} \tag{3}$$

The compliance matrix of the flexure-based mechanism can be obtained by

transform the compliance matrix of each flexure hinge from the local coordinate O_i-XYZ to the global coordinate O-XYZ. The matrix transformation is listed in the Eq. (4). Where, P_i and R_i are the translation matrix and rotation matrix, respectively.

$$C_i = \begin{bmatrix} R_i & 0 \\ 0 & R_i \end{bmatrix} \begin{bmatrix} I & P_i^T \\ 0 & I \end{bmatrix} C_0 \begin{bmatrix} I & 0 \\ P_i & I \end{bmatrix} \begin{bmatrix} R_i^T & 0 \\ 0 & R_i^T \end{bmatrix} \qquad i = 1 \cdots 6 \tag{4}$$

For the ith flexure hinge, $P_i = \begin{bmatrix} 0 & -r_{iz} & r_{iy} \\ r_{iz} & 0 & -r_{ix} \\ -r_{iy} & r_{ix} & 0 \end{bmatrix}$, $\boldsymbol{r}_i = \overrightarrow{o_i o} = \begin{bmatrix} r_{ix} & r_{iy} & r_{iz} \end{bmatrix}$ is the vector from the origin O_i to the global origin O in the local coordinate O_i-XYZ. R_i is the rotation matrix of the coordinate O_i-XYZ with respect to O-XYZ, which is decided by the rotation axis. The rotation matrixes about the X, Y and Z axis are

$$R_x(\theta_x) = \begin{bmatrix} 1 & 0 & 0 \\ 0 & \cos\theta_x & -\sin\theta_x \\ 0 & \sin\theta_x & \cos\theta_x \end{bmatrix}, \quad R_y(\theta_y) = \begin{bmatrix} \cos\theta_y & 0 & \sin\theta_y \\ 0 & 1 & \\ -\sin\theta_y & 0 & \cos\theta_y \end{bmatrix}, \quad R_z(\theta_z) = \begin{bmatrix} \cos\theta_z & -\sin\theta_z & 0 \\ \sin\theta_z & \cos\theta_z & 0 \\ 0 & 0 & 1 \end{bmatrix},$$

respectively.

According to the structure of the flexure-based mechanism, the flexure hinges in the left and right side of the mechanism are connected in parallel. Four leaf-spring hinges are parallel connected and then series connected with the right circular hinge in the left side. In the calculation of the entire flexure-based mechanism, the compliance matrix in serial chain and the stiffness matrix in parallel connection can be added directly. Thus, the compliance matrix of the designed flexible mechanism can be obtained as

$$C = \left\{ \left[\left(\sum \left(C_i^{-1} \right) \right)^{-1} + C_1 \right]^{-1} + C_2^{-1} \right\}^{-1} \qquad i = 3, 4, 5, 6 \tag{5}$$

The displacement of the flexure-based mechanism can be calculated by the Eq. (6).

$$S = CF \tag{6}$$

where, $S = \begin{bmatrix} x & y & z & \theta_x & \theta_y & \theta_z \end{bmatrix}$, $F = \begin{bmatrix} F_x & F_y & F_z & M_x & M_y & M_z \end{bmatrix}$

According to the operating principle of the linear actuator, the displacement of the operating point O in the X direction is used to drive the slider, which decides the final motion of the slider. Under the function of force F_y from the PZT, the flexure-based mechanism generates displacements x and y in the X and Y directions,

respectively. The amplification ratio of the flexure-based mechanism can be calculated as

$$AMP_1 = \frac{x}{y} \tag{7}$$

3.2 Kinematic analysis

In the kinematic analysis, it is obvious that both the input and output points locate on the connecting rod 8. Considering the rigidity of the rod 8, it will rotate about the center of the flexure hinge 2 under the function of the input displacement, which is shown in Fig. 5. The input displacement is defined as y_{in}, the lateral displacement x_{out} of the operating point O can be easily obtained according to the geometrical knowledge of similar triangles. Thus, another amplification ratio can be obtained based on the kinematic property of the flexure-based mechanism.

$$AMP_2 = \frac{x_{out}}{y_{in}} = \frac{h}{w} \tag{8}$$

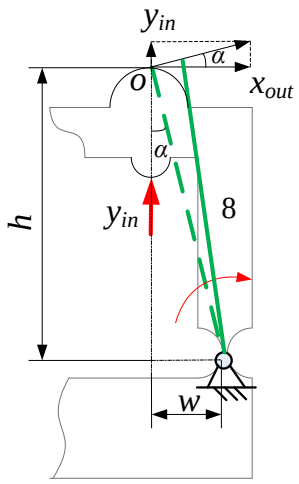

Fig. 5 Kinematic model

3.3 Optimization of the flexure-based mechanism

There have been rich experiences in the design of single right circular flexure hinge or leaf-spring flexure hinge, thus, the parameters of single flexure hinges shown in Fig. 4 are designed as $b_c = b_l = 10$ mm, $t_c = t_l = 0.5$mm, $r = 2.5$mm, other sizes can be seen in Fig. 6. According to the compliance analysis, p, q and l are related to the compliance transform matrix, which also have important influence on the static property of the flexure-based mechanism. Besides, they directly determine the compactness of the entire flexure-based mechanism. Therefore, these three variables

are optimized in the flowing text.

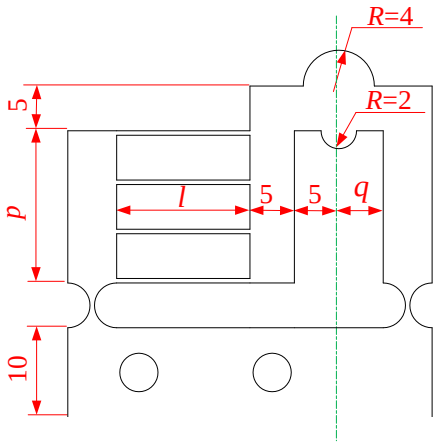

Fig. 6 The sizes of the flexure-based mechanism.

In order to optimize the sizes of p, q and l, the output displacement of the operating point under the function of the fore F_y =10 N are analyzed based on Eq. (6). A series of sizes of p, q and l are selected: p = [8, 11, 14, 17, 20, 23], q = [5, 10, 15, 20, 25], l = [5, 10, 15, 20, 25]. The displacements of the operating point O in the X and Y directions are shown in Fig. 7. It can be seen that the p has little influence on the Y-direction displacement, but the X-direction displacement increases linearly as p increases. The displacements in both X and Y directions rise with the increase of the q and l, but the increasing rates are obviously different. Thus, the *AMPs* of the mechanism with the three variables are further analyzed, which are shown in Fig. 8.

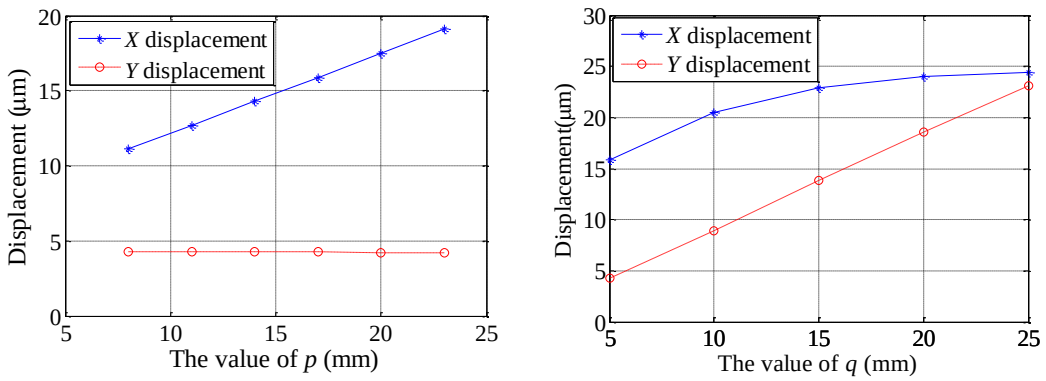

(a) (b)

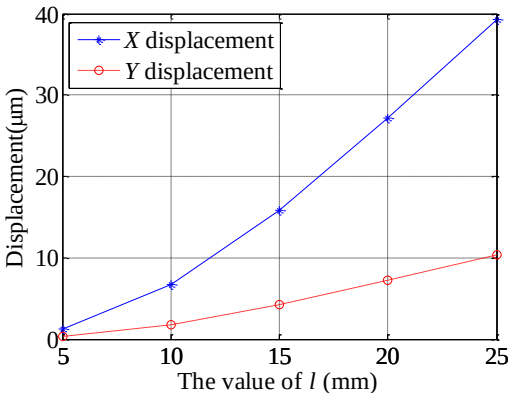

(c)

Fig. 7 The outputs of the flexure-based mechanism in the *X* and *Y* directions with different variables. (a) The variable *p*. (b) The variable *q*. (c) The variable *l*.

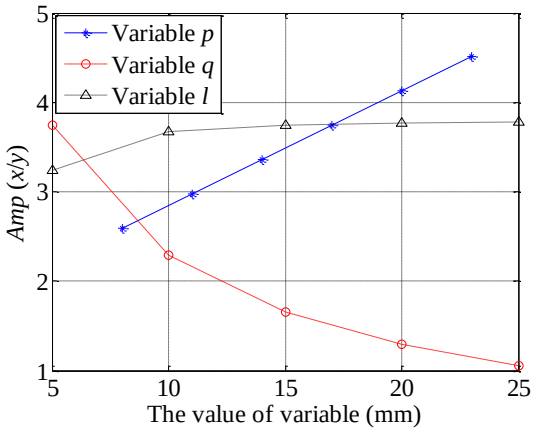

Fig. 8 The amplification ratios of the flexure-based mechanism with different values of variables.

A larger amplification ratio can enlarge the output of the slider in single step, further leads to a higher velocity. Thus, in order to ensure a larger amplification ratio, the value of *p*, *l* should be bigger and *q* is better to be small. However, a larger *p* or *l* makes the flexure-based mechanism loose, and the impact of *l* on the amplification ratio is very limited. Considering the amplification ratio and the compactness of the mechanism, the sizes of the proposed flexure-based mechanism are selected as Table 1.

Table 1 The sizes of the flexure-based mechanism

Parameters	Value (mm)
p	17
l	15
q	5
b_c=b_l	10
t_c=t_l	0.5
r	2.5

4. Finite Element Analysis

Finite Element Analysis (FEA) is implemented on the proposed flexure-based mechanism to validate the correctness of theoretical analysis. The material is aluminum alloy with Young's modules E = 71 GPa, density ρ = 2770 kg/m^3, and Poisson's ratio v= 0.33.

The input force F = [0, 10, 0, 0, 0, 0] is applied on the driving point to observe the deformation of the flexure-based mechanism. As shown in Fig. 9, the mechanism deformed as the design objective, the operating point generates the output displacements in both X and Y direction with values of 14.88 μm and 4.35 μm, respectively. It indicates that the proposed flexure-based mechanism can drive the slider move in the X direction. The amplification ratio is 3.42 in the FEA, which agrees well with the theoretical analysis of 3.74 in static analysis and 3.67 in kinematic analysis.

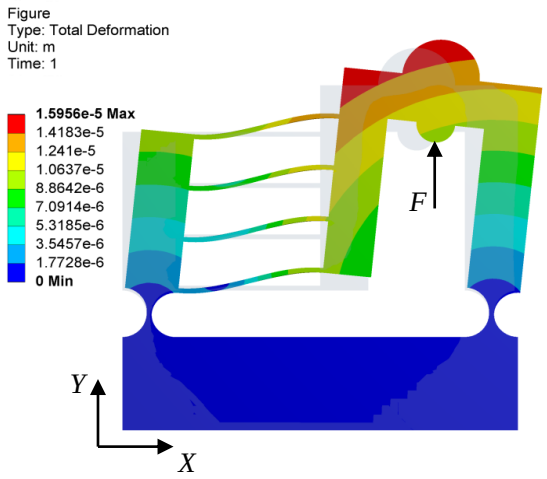

Fig. 9 The deformation of the flexure-based mechanism in FEA

The first three mode shapes of the flexure-based mechanism are shown in Fig. 10.

The first mode shape is along the working direction in the *XY* plane. The second and third mode shapes are out of the plane, which is harmful for the kinematic precision. According to the FEA, the first three natural frequencies of the mechanism are 942.71Hz, 2829.5Hz and 6149.7Hz, respectively. The second and third natural frequencies are much higher than the first natural frequency, which means the second and third mode shape is hard to activate in low frequency operation.

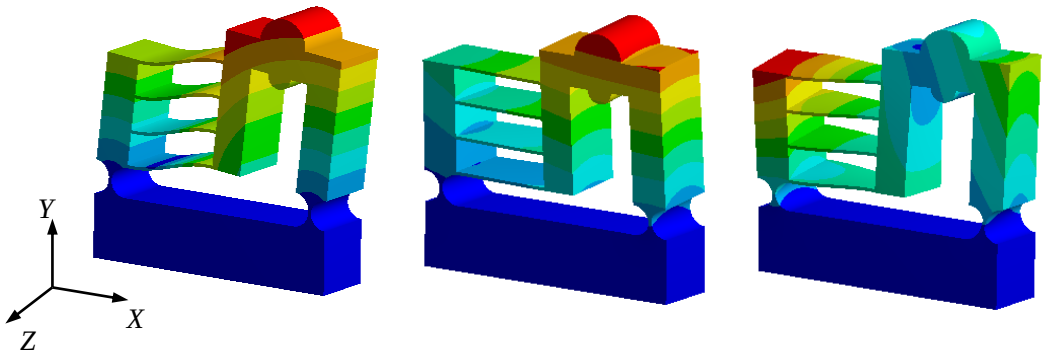

Fig. 10 The first three mode shapes of the flexure-based mechanism.

5. Experimental investigation

5.1 The modified sawtooth wave

The traditional sawtooth wave is usually selected as the driving signal in the stick-slip motion, but how to constrain the vibration of the runner and improve the velocity are still challenging. Based on this fact, a modified sawtooth wave is proposed, which is shown in Fig. 11 (b). Compared with the traditional sawtooth wave, the fall curve of the modified sawtooth is a cycloid. The mathematic models of the two kinds of signals are respectively given in Eq. (9) and Eq. (10), which can be multiplied by a constant number to obtain any magnitudes of voltages.

$$V_{\mathrm{tra}}(t)=\begin{cases} k_1 t & t \le t_1 \\ -10\dfrac{(t-t_1)}{t_2-t_1}+10 & t_1 < t \le t_2 \end{cases} \tag{9}$$

$$V_{\mathrm{mod}}(t)=\begin{cases} k_1 t & t \le t_1 \\ -10\left[\dfrac{t-t_1}{t_2-t_1}-\dfrac{1}{2\pi}\sin\left(2\pi\dfrac{t-t_1}{t_2-t_1}\right)\right]+10 & t_1 < t \le t_2 \end{cases} \tag{10}$$

where, k_1 is a variable coefficient, the value should satisfy $k_1 t_1 = 10$ for different t_1.

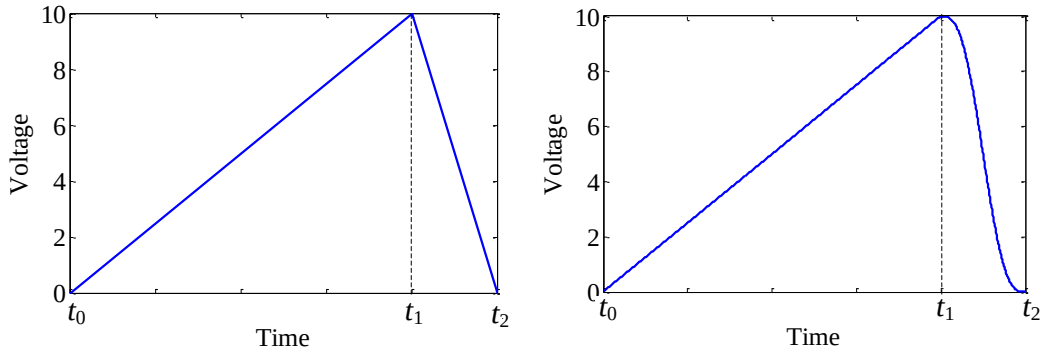

Fig. 11 The driving signal. (a) The traditional sawtooth wave. (b) The modified swatooth wave.

5.2 The experimental setup

As shown in Fig. 12, the flexure-based mechanism is monolithically manufactured from an Aluminum Alloy T7075 using the Wire Electric Discharge Machining (WEDM), the boundary dimensions are 41mm×42mm×10mm. A manual coarse mobile platform (Winner Optical Instrument, WN115TM50M) is used to preload the micropositioner and the slider in initial state. A piezoelectric (THORlabs, AE0505D18F) is employed as the micropositioner actuator. The nominal maximal displacement of such kind of piezoelectric is 15 μm in 100V. The piezoelectric is driven by a PI E-505.00 piezoelectric amplifier, which has a constant amplification factor 10. Two laser displacement sensors (KEYENCE, LK-H050) are utilized to measure the displacements of the flexure-based mechanism in the *Y* direction and the slider in the *X* direction, respectively. A dSPACE DS1103 R&D control board is utilized to provide I/O interfaces with a sampling rate of 20 KHz. The loads are weighted by a precision electronic balance in a container, and then loaded on the slider though a line of aluminum and a fixed pulley. In the experiments, the locking force is defined as the largest force that the actuator can hold, a pull-push force gauge (NK20) is used to measure the locking force by pulling or pushing the slider until the slider has a stable movement.

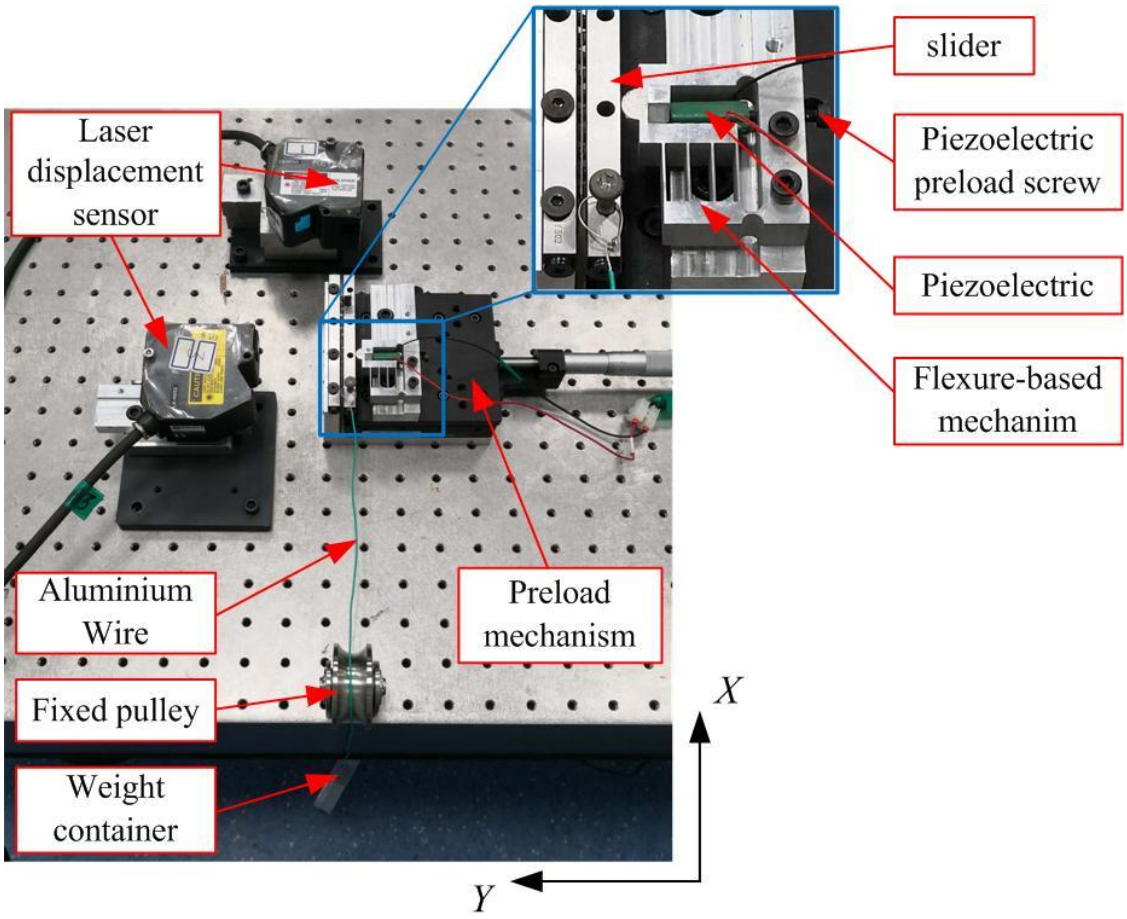

Fig. 12 The experimental setup.

5.3 The experimental results and analyses

A triangular wave with voltage 100 $V_{p\text{-}p}$ is input into the PZT to examine the displacement amplification ratio of the prototype. The rise and fall times of the wave are set as 3 s. The locking force is 5 N. Two laser displacement sensors measure the displacements in the *Y* and *X* directions, respectively. The experimental results shown in Fig. 13 indicate that the amplification ratio is about 3.16, which agrees well with the theoretical and FEA results.

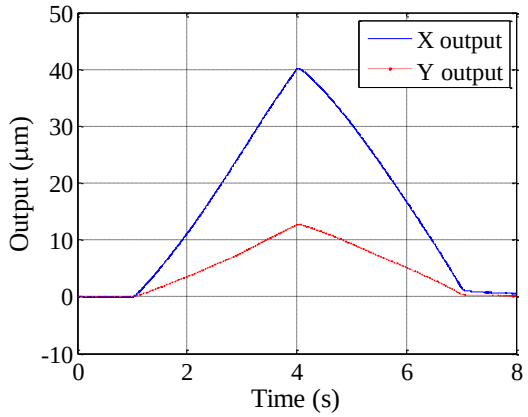

Fig. 13 The outputs of the linear actuator in single step.

After many experimental trials, a stairstep signal with 0.5 V magnitude is input into the PZT to observe the resolution of the proposed linear actuator, as shown in Fig. 14, it indicates that the resolution is about 60 nm.

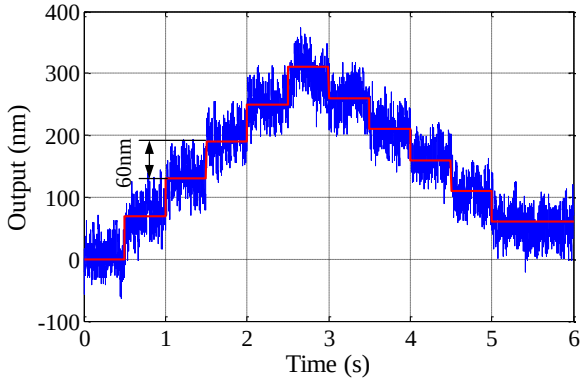

Fig. 14 The resolution of the linear actuator

In the velocity test of the slider for different voltages, the driving frequency is 1 Hz. Fig. 15 shows the velocity of the slider in the driving of the traditional and modified sawtooth waves. The velocity increases as the voltage increases for both signals, but the modified sawtooth always has a higher velocity. In order to obtain the maximal velocity, the voltage 100 V is selected in the following experiments.

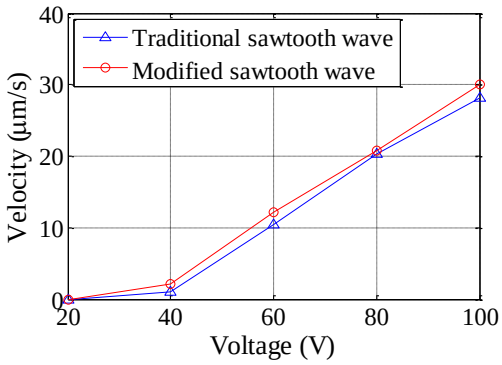

Fig. 15 The velocity of the slider with different voltages in the driving of the traditional and modified sawtooth waves

The retraction time of the piezoelectric affects the vibration and backward displacements of the slider greatly, thus, the traditional and modified sawtooth waves are set with three different contraction times of 0.2 ms, 0.4 ms and 0.6 ms. The outputs of the slider after five cycles are measured. As shown in Fig. 16(a), both signals increase the output with the reduction of the contraction time. Under five cycles driving of the traditional and modified sawtooth waves, the outputs are 140.8 μm, 150.2 μm, 91.0 μm, 123.7 μm, and -4.5 μm, 91.5 μm, respectively. The negative may be caused by the fact that the stick phenomenon still exist in the retraction phase, and the inertia of the slider is larger than the extension phase due to the high speed. The modified sawtooth wave obviously output larger displacement, especially in the longer retracting time. The gap between the traditional and modified sawtooth increases from 9.4 μm to 96 μm as the retraction time increases, which indicates the proposed modified sawtooth is more efficient in the slower contraction.

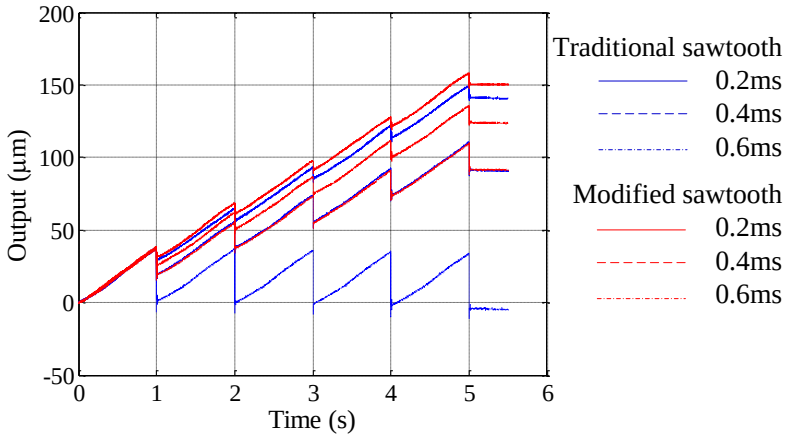

(a)

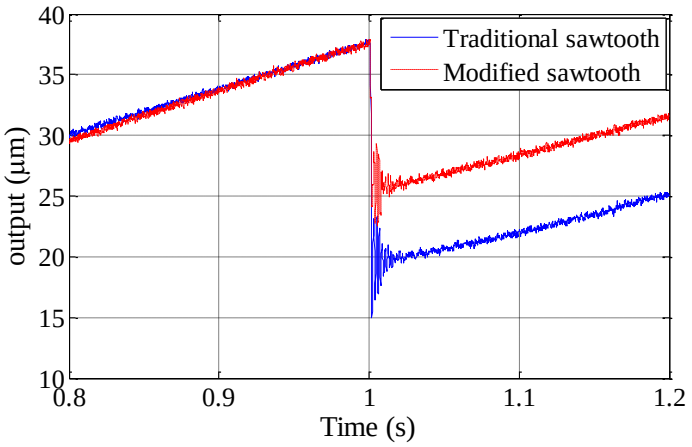

(b)

Fig. 16 The outputs of the slider with the traditional and modified sawtooth waves. (a) The outputs of the slider after 5 cycles. (b) The outputs of the slider in the first step

In order to compare the maximal overshoot and backward displacement of the slider, the outputs of the slider in the first step with contraction time 0.4 ms are shown in Fig. 16(b). In the driving of the traditional and modified sawtooth waves, the maximal overshoot is reduced from 5 μm to 3 μm, the backward displacement reduced from 17.5 μm to 11.5 μm. These results demonstrate that the proposed modified sawtooth wave can be used to improve the output property of the linear actuator.

Fig. 17 shows the velocity of the slider with different driving frequencies. The fall time of both signals are set as 0.2 ms. The experiments show that the velocities reach the largest when the frequency is about 500 Hz, which are 25.2 mm/s and 26.2 mm/s, respectively for the traditional and modified sawtooth wave. The modified sawtooth has larger velocity in each frequency, and the velocity in 300 Hz is about 1.35 times larger than that of the traditional sawtooth. The velocities of both signals are reduced after 500 Hz, the possible reason is that the extension time of piezoelectric is so short that it cannot extend to the theoretical length.

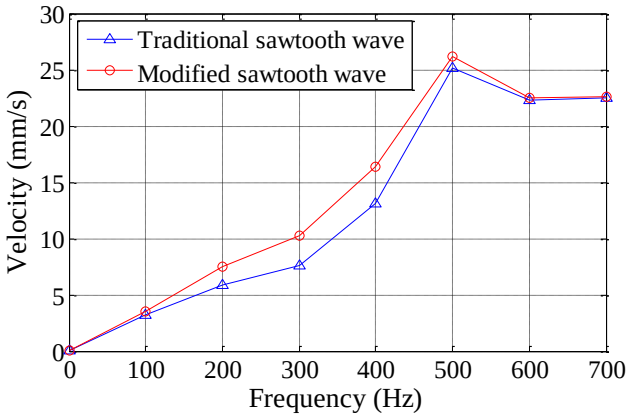

Fig. 17 The velocity with different frequencies

Besides the inherent parameters of the linear actuator, the external loads also affect the output of the slider. Three locking force 3N, 5N and 7N are selected in this experiment, and the driving frequency is 1 Hz. In the driving of traditional sawtooth, Fig. 18(a) shows the relationship between the load and velocity with different locking force. It indicates that a larger locking force has better loading capacity and slower reduction of velocity, but the smaller locking force output faster in the light load. Furthermore, with the locking force 5 N, the output velocity in the driving of the traditional and modified sawtooth waves are compared. As shown in Fig. 18(b), it is obvious that the modified sawtooth has larger velocity in different loads.

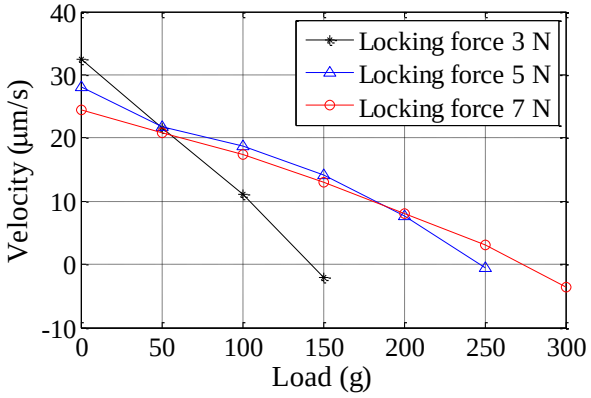

(a)

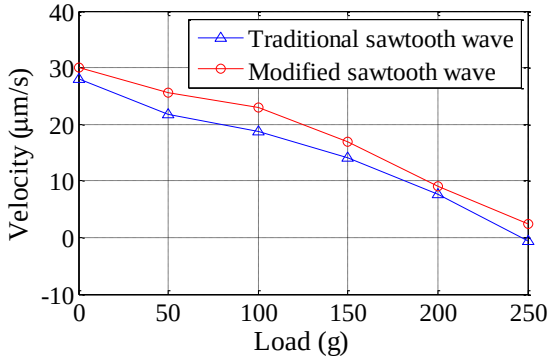

(b)

Fig. 18 The testing of the loading capacity. (a) The loading capacity with different locking force. (b) The loading capacity with locking force 5 N.

Conclusion

A piezoelectric driven asymmetric flexure-based mechanism was proposed, which generated the axial motion and the lateral motion, the former increased the pressure between the micropositioner and the slider in the extension phase, and reduce the pressure in the contraction phase, the latter driven the slider. The amplification coefficient of the flexure-based mechanism was analyzed through the static and kinematic analysis, and then the flexure-based mechanism was optimized based on the compliance matrix. Finite Element Analysis validated the flexure-based mechanism could realize the expected motion. The amplification coefficient of the flexure-based mechanism is 3.74, 3.67, 3.42 and 3.16 from the static analysis, kinematic analysis, FEA and the experiment, respectively, indicating the correctness of the theoretical analysis. The resolution of the developed linear actuator is about 60nm.

Based on the traditional sawtooth wave, a modified sawtooth wave with a cycloid fall curve was designed. According to the experimental results, the modified sawtooth wave generated larger velocity than the traditional sawtooth wave in same voltages, fall times, frequencies and loads. The overshoot and backward displacements were also smaller for the modified sawtooth wave. Under the driving of the modified sawtooth wave, the maximal velocity reached 26.2 mm/s, a maximum load of 250 g is achieved with locking force 5 N. All these results verified that the proposed linear actuator was able to realize precision motion, and the modified sawtooth wave had better output properties.

Acknowledgements

This research is supported by National Natural Science Foundation of China (Nos. 51675371, 51675367, 51675376), EU H2020 MNR4SCell (No. 734174), Joint Funds of the National Natural Science Foundation of China & Civil Aviation Administration of China (No. U1833106).

References

[1] Y. Yan, Y. Geng, Z. Hu. Recent advances in AFM tip-based nanomechanical machining. International Journal of Machine Tools & Manufacture, 2015, 99: 1–18.

[2] Z. Guo, Y. Tian, X. Liu, et al. Experimental investigation of the tip based micronano machining. Applied Surface Science, 2017, 426: 406-417.

[3] Y. Yong, B. Bhikkaji, S. Moheimani. Design, modeling, and FPAA-based control of a high-speed atomic force microscope nanopositioner. IEEE/ASME Transactions on Mechatronics, 2013, 18(3): 1060-1071.

[4] M. Li, L. Liu, N. Xi and Y. Wang. Applications of micro/nano automation technology in detecting cancer cells for personalized medicine. IEEE Transactions on Nanotechnology, 2017, 16(2): 217-229.

[5] S. Hong, J. Kim, H. Park, et al. Influence of Zr content on phase formation, transition and mechanical behavior of Ni-Ti-Hf-Zr high temperature shape memory alloys. Journal of Alloys and Compounds, 2017, 692: 77-85.

[6] X. Tan and J. S. Baras. Modeling and control of hysteresis in magnetostrictive actuators. Automatica, 2004, 40(9): 1469-1480.

[7] Q. Xu. New flexure parallel-kinematic micropositioning system with large workspace. IEEE Transactions on Robotics, 2012, 28(2): 478-491.

[8] J. Shang, Y. Tian, Z. Li, et al. A novel voice coil motor-driven compliant micropositioning stage based on flexure mechanism. Review of Scientific Instruments, 2015, 86 (9): 095001.

[9] K. Cai, Y. Tian, F. Wang, et al. Development of a piezodriven 3-DOF stage with T-shapeflexible hinge mechanism. Robotics and Computer-Integrated Manufacturing, 2016, 37 (1): 125–138.

[10] L. Lai, G. G, L. Zhu. Design and control of a decoupled two degree of freedom translational parallel micro-positioning stage. Review of Scientific Instruments, 2012, 83(4): 045105.

[11] Z. Guo, Y. Tian, X. Liu, et al. Design and control methodology of a 3-DOF flexure based mechanism for micro/nano positioning. Robotics and Computer Integrated Manufacturing, 2015, 32: 93–105.

[12] K. Cai, Y. Tian, F. Wang, et al. Modeling and controller design of a 6-DOF precision positioning system. Mechanical Systems and Signal Processing, 2017, 104: 536-555.

[13] Y. Qin, B. Shirinzadeh, Y. Tian, D. Zhang, U. Bhagat, L. Clark. Design and computational optimization of a decoupled 2-DOF monolithic mechanism. IEEE/ASME Transactions on Mechatronics, 2014,19(3): 872-881.

[14] Y. Yong, S. Aphale, S. RezaMoheimani. Design, identification, and control of a flexure-based xy stage for fast nanoscale positioning. IEEE Transactions on Nanotechnology, 2009, 8(1): 46-54.

[15] H. Kim, D. Gweon. Development of a compact and long range XYθz nanopositioning stage. Review of Scientific Instruments, 2012, 83(8): 085102.

[16] Y. Tian, B. Shirinzadeh, D. Zhang, et al. Development and dynamic modelling of a flexure-based Scott-Russell mechanism for nano-manipulation. Mechanical Systems and Signal Processing, 2009, 23(3): 957-978.

[17] D. Hwang, M. Lee, J. Jeong. Note: Design of a novel ultraprecision in-plane XYθ positioning stage. Review of Scientific Instruments, 2011, 82(2): 026102.

[18] S. Salisbury, D. Waechter, R. Mrad, et al. Design considerations for complementary inchworm actuators. IEEE/ASME Transactions on Mechatronics, 2006, 11(3): 265–272.

[19] P. Tenzer, R. Mrad. A Systematic Procedure for the Design of Piezoelectric Inchworm Precision Positioners. IEEE/ASME Transactions on Mechatronics, 2004, 9: 427~435.

[20] J. Li, H. Zhao, H. Qu, et al. A piezoelectric-driven rotary actuator by means of inchworm motion. Sensors and Actuators A: Physical, 2013, 194: 269-276.

[21] J. Li, H. Zhao, X. Qu, et al. Development of a compact 2-DOF precision piezoelectric positioning platform based on inchworm principle. Sensors and Actuators A: Physical, 2015, 222: 87-95.

[22] S. Shao, S. Song, N. Chen, et al. Structure and control strategy for a piezoelectric inchworm actuator equipped with MEMS ridges. Sensors and Actuators A: Physical, 2017, 264: 40-50.

[23] C. Chu, S. Fan. A novel long-travel piezoelectric-driven linear nanopositioning stage. Precision Engineering, 2006, 30: 85–95.

[24] Y. Peng, J. Cao, Z. Guo, et al. A linear actuator for precision positioning of dual objects, Smart Material Structure, 2015, 24: 125039.

[25] T. Cheng, M. He, H. Li, et al. Investigation on driving characteristics of a piezoelectric stick–slip actuator based on resonant/off-resonant hybrid excitation. Smart Materials and Structures, 2017, 26: 035042.

[26] J. Peng, X. Chen. Modeling of piezoelectric-driven stick–slip actuators. IEEE/ASME Transactions on Mechatronics, 2011, 16(2): 394-399.

[27] M. Hunstig, T. Hemsel, and W.Sextro. Modelling the friction contact in an inertia motor. Journal of Intelligent Material Systems and Structures, 2013, 24(11):1380–1391.

[28] M. Zhou, Z. Fan, Z. Ma, et al. Design and experimental research of a novel stick-slip type piezoelectric actuator. Micromachines, 2017, 8(5): 150.

[29] J. Li, X. Zhou, H. Zhao, et al. Design and experimental performances of a piezoelectric linear actuator by means of lateral motion. Smart Materials and Structures, 2015, 24: 06500.

[30] T. Cheng, M. He, H. Li, et al. A novel trapezoid-type stick–slip piezoelectric linear actuator using right circular flexure hinge mechanism. IEEE Transactions on Industrial Electronics. 2017, 64(7): 5545-5552.

[31] H. Nguyen, E. Teidelt, V. Popov, et al. Modeling and waveform optimization of stick–slip micro-drives using the method of dimensionality reduction. Archive of Applied Mechanics, 2016, 86(10): 1771-1785.